Nanoscale

Infrared Color-Sorting Metasurface

Journal:	*Nanoscale*
Manuscript ID	NR-ART-05-2024-001891.R1
Article Type:	Paper
Date Submitted by the Author:	07-Jun-2024

Complete List of Authors:	Chen, Guanghao; UCSD, Electrical and Computer Engineering Zhou, Junxiao; UCSD, Electrical and Computer Engineering Chen, Li; UCSD, Materials Science and Engineering Tian, Fanglin; UCSD, Electrical and Computer Engineering Liu, Zhaowei; University of California, San Diego, Electrical and Computer Engineering

Infrared Color-Sorting Metasurface: Data Availability Statement

GUANGHAO CHEN[1+], JUNXIAO ZHOU[1+], LI CHEN[2], FANGLIN TIAN[1], ZHAOWEI LIU[1,2*]

[1]*Department of Electrical and Computer Engineering, University of California, San Diego, 9500 Gilman Drive, La Jolla, California 92093, United States*
[2]*Department of Materials Science and Engineering, University of California, San Diego, La Jolla, California 92093, United States*
* *zhaowei@ucsd.edu*
[+]*These authors contributed equally to this work.*

The data supporting this article have been included as part of the Supplementary Information.

Infrared Color-Sorting Metasurface

GUANGHAO CHEN[1+], JUNXIAO ZHOU[1+], LI CHEN[2], FANGLIN TIAN[1], ZHAOWEI LIU[1,2*]

[1]*Department of Electrical and Computer Engineering, University of California, San Diego, 9500 Gilman Drive, La Jolla, California 92093, United States*
[2]*Department of Materials Science and Engineering, University of California, San Diego, La Jolla, California 92093, United States*
* *zhaowei@ucsd.edu*
[+]*These authors contributed equally to this work.*

Abstract: The process of sorting light based on colors (photon energy) is a prerequisite in broadband optical systems, typically achieved in the form of guiding incoming signals through a sequence of spectral filters. The assembly of filters often leads to lengthy optical trains and consequently, large system footprints. In this work, we address this issue by proposing a flat color-sorting device comprised of a diffraction grating and a dielectric Huygens' metasurface. Upon the incidence of a broadband beam, the grating disperses wavelengths to a continuous range of angles in accordance with the law of diffraction. The following metasurface with multiple paired Huygens' resonances corrects the dispersion and binds wavelengths to the corresponding waveband with a designated output angle. We demonstrate the efficacy by designing a color-sorting metasurface with two discrete dispersion-compensated outputs (10.8 ± 0.3 μm and 11.9 ± 0.3 μm), based on the proposed approach. The optimized metasurface possesses an overall transmittance exceeding 57% and reduces lateral dispersion by 90% at the output. The proposed color-sorting mechanism provides a solution that benefits the designing of metasurface for miniature multi-band systems.

1. INTRODUCTION

In optical systems, color sorting is a fundamental process that partitions broadband photon energy into multiple sub-bands spectrally. This procedure find utility in various applications, including optical networks (1), spectroscopy (2, 3), and microscopy (4). Arrays of spectral filters with steep roll-offs are commonly employed for this purpose, often resulting in lengthy and bulky catadioptric optical trains (5, 6). Optical metasurfaces, utilizing artificially designed structures with subwavelength dimensions, effectively manipulate electromagnetic fields on smaller scales (7-9). This presents a promising platform for developing compact and lightweight optical elements with diverse functionalities (10, 11), including examples such as metalens (12, 13), beam shaping (14-16), edge detection (17-22), quantitative phase imaging, and more (23-28). Over the past decade, publications and industrial applications have showcased metasurface-based devices and systems significantly smaller than the conventional counterparts (29-31). Many of them are plagued by severe chromatic aberrations arose from diffraction and unsuitable for broadband illumination. Consequently, metasurface achromatism became a topic of considerable research interest in the past decade. Notably, achromatic devices such as achromatic metalenses (32-38), achromatic metasurface steerers (39-41), and metasurface dispersion correctors have been explored (42, 43). Different from the purpose of sorting colors, these metasurfaces are only required to steer beam achromatically and refract all wavelengths to the same direction, achieved by a spatial-varying dispersion correction introduced to the incident waves via a monolayer of nano-resonators, also known as meta-atoms (44-46). Despite its effectiveness in single-band devices, this method falls short in color-sorting where the broadband input should be separated and directed achromatically to discrete sub-bands. The latter requires ideas to simultaneously provide dedicated dispersion correction profiles to the corresponding sub-bands, which exceeds the capacity of natural optical materials and reported metasurface designs.

Acknowledging this challenge, in this work, we propose a color-sorting mechanism that produces waveband-dependent dispersion correction, and building upon this approach, we demonstrate a metasurface color-sorter for two infrared sub-bands, 10.8 ± 0.3 μm and 11.9 ± 0.3 μm. As schematically shown in Fig. 1(a), the color-sorting device combines the dispersion of a grating and the correction capability of a multi-layer dielectric Huygens' metasurface. The diffraction grating disperses the incoming wavelengths indiscriminately, followed by a metasurface correcting the dispersion in the waves. As a result of the correction, photons are sorted to the corresponding sub-band minimized dispersion at the device output. Figure 1(b) provides a zoom-in view of the metasurface, showing multiple layers of high-refractive-index meta-atom arrays embedded in a low-refractive-index host medium. Although presented separately in the purpose of highlighting their individual roles, the grating and metasurface in Fig. 1 (a) can be fabricated back-to-back seamlessly to form an ultrathin device.

In the rest of this work, we begin by explaining the proposed color-sorting mechanism in Section 2. Next, in Section 3, we demonstrate the process of designing and optimizing a dual-band color-sorting metasurface, along with

analysis and optical performance estimation. Finally in Section 4, the proposed methodology is discussed and followed by the conclusion of our work.

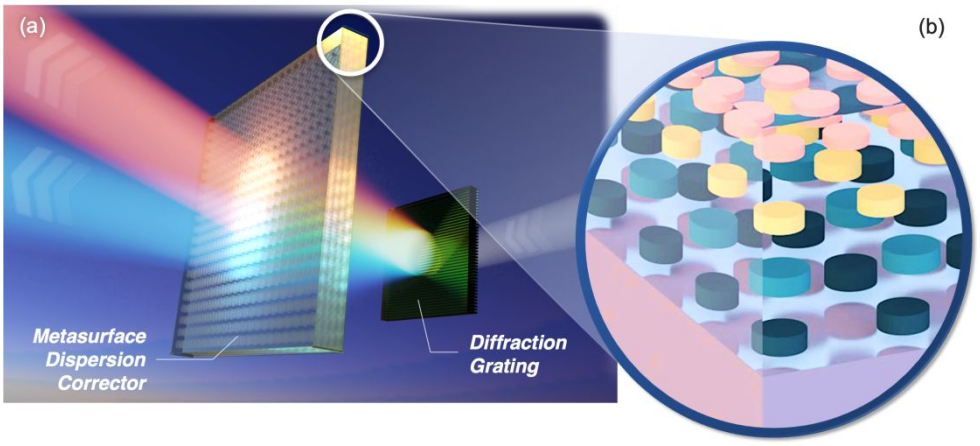

Fig. 1. A schematic of the proposed dual-band color-sorter design. A broadband signal (white color, on the right side of (a)) is spread by a grating and then binned into two discrete angles for each band (pink and blue colors on the left side of (a)) as it passes through the metasurface dispersion corrector. The metasurface can be fabricated on top of the grating. Here they are separated for convenience. (b) A zoom-in view that illustrates multi-layer disk-shaped nano-resonators in the dielectric metasurface.

2. THEORY

In this design, we utilize the Mie resonances in dielectric nanostructures to produce the required dispersion correction. Specifically, we opt for dielectric Huygens' resonators, owing to their high efficiency, low-aspect-ratio profiles, and a simpler fabrication process compared to high-n waveguide metasurfaces (34). In a Huygens' meta-atom, the electrical dipole (ED, with the subscript e) and magnetic dipole (MD, subscripted as m) resonances dominate at small size parameters (47, 48). The transmission coefficient of a periodic meta-atom array is given by (49):

$$t(\omega) = 1 + \frac{2i\gamma_e\omega}{\omega_e^2 - \omega^2 - 2i\gamma_e\omega} + \frac{2i\gamma_m\omega}{\omega_m^2 - \omega^2 - 2i\gamma_m\omega} \tag{1}$$

Here, $\gamma_{e,m}$ is the damping factor and $\omega_{e,m}$ denotes the resonance frequency. At the first Kerker's condition (50), i.e., $\omega_e \approx \omega_m \approx \omega_0$ and $\gamma_e \approx \gamma_m \approx \gamma$, both the transmission and the dispersion are maximized simultaneously at the resonant frequency. The dispersion is strong near the resonance of a Huygens' dipole and drops rapidly as the resonance shifts away. To observe the dispersion near the resonance more clearly, we express the parameters in Eq. (1) in terms of ω_0, i.e., $\gamma' = \gamma\omega_0$ and $\omega = (1 + x)\omega_0$. The scaled group delay (GD) is, therefore,

$$\phi'(x,\gamma') = -\frac{4\gamma'(2 + x(2 + x))}{4\gamma'^2(1 + x)^2 + x^2(2 + x)^2} \tag{2}$$

The corresponding scaled group delay dispersion (GDD) is given by Eq. (B4) in Note B in the supplementary information (SI). In this application, $x \in [-0.028, 0.028]$, i.e., the bandwidth is $0.056\omega_0$ centered at ω_0. The GD and GDD are illustrated by the mesh surfaces in Fig. 2 (a) and (b), respectively. Flattening $\phi'(x,\gamma')$ within x is equivalent to reducing $|\phi''(x,\gamma')|$ to zero. Since only one degree of freedom is provided, $\phi'(x,\gamma')$ and $\phi''(x,\gamma')$ are coupled. As γ' increases, the magnitudes of GDD and GD are reduced in unison.

Here, we solve this problem by strategically combining the resonances from two Huygens' meta-atoms. As $\phi''(x,\gamma')$ is roughly anti-symmetric near $\phi''(x,\gamma')|_{x=0}$, in the presence of another Huygens' resonance, the left half $(x < 0)$ of one resonance with positive GDD cancelling the right half $(x > 0)$ of the other resonance with negative GDD. As a result, the summed GDD for the sub-band between these two Huygens' resonances can be reduced, while the GD increases from both resonances adding up in the same direction. Hereafter, these two specially matched Huygens' resonances are referred to as "paired Huygens' resonances". Mathematically, the additional Huygens' resonance provides another degree of freedom that uncouples the modification of $\phi'(x,\gamma')$ and $\phi''(x,\gamma')$:

$$\phi'(\omega;\gamma_1,\gamma_2,\omega_1,\omega_2) = \phi'(\omega;\gamma_1,\omega_1) + \phi'(\omega;\gamma_2,\omega_2)$$
$$= -\frac{4\gamma_1(\omega_1^2-\omega^2)}{\omega_1^4+4\gamma_1^2\omega^2-2\omega_1^2\omega^2+\omega^4} - \frac{4\gamma_2(\omega_2^2-\omega^2)}{\omega_2^4+4\gamma_2^2\omega^2-2\omega_2^2\omega^2+\omega^4} \quad (3)$$

Again, we substitute the variables as described in Eq. (B6) in Note B in the SI and observe the GD and GDD in the vicinity of the sub-band center between the paired Huygens' resonances. As shown by the GD function (mesh surface) in Fig. 2 (c), the single Huygens' resonance exhibits increased dispersion as the damping vanishes, taking the form of a typical Lorentzian spectral shape curve on the frequency axis. The corresponding GDD is depicted by the mesh surface in Fig. 2 (d). Likewise, the GD and GDD of the paired Huygens' resonances are displayed in the respective coordinates as solid surfaces.

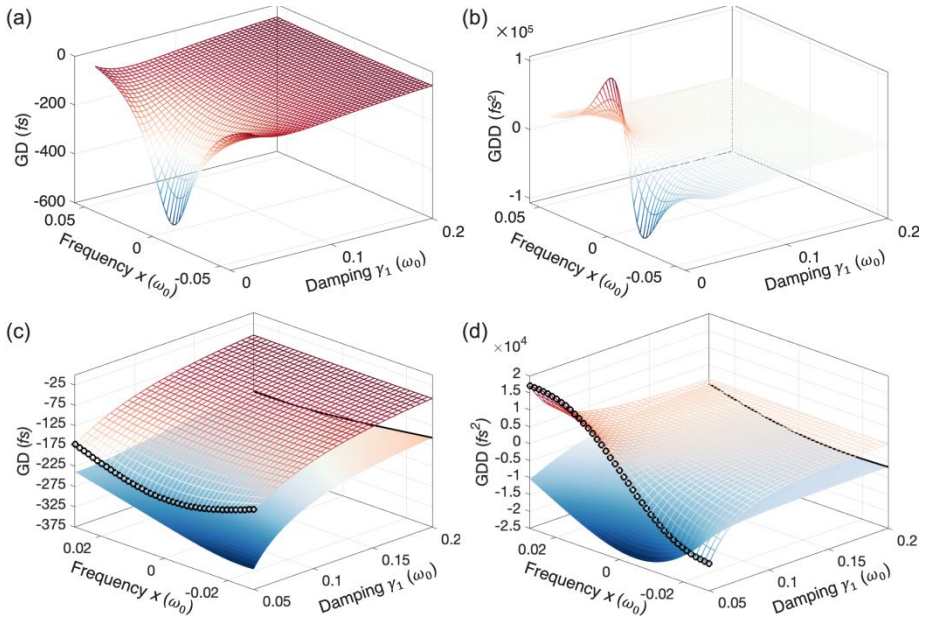

Fig. 2. The group delay (GD) and group delay dispersion (GDD) of a Huygens' resonance. (a) and (b) GD and GDD of a single Huygens' resonance. (c) and (d) Compare GD and GDD of paired Huygens' resonances (solid surfaces) to parts of (a) and (b) (mesh surface). The paired resonances produce the same GD with a much smaller GDD. The resonance offset parameter δ and damping parameter γ_2 are set to 0.06 and 0.1, respectively.

Here, we freeze the resonance offset parameter δ (see Note B in the SI for the definition) and the damping parameter γ_2 at 0.06 and 0.1, respectively, and observe changes in GD and GDD as γ_1 varies. Overall, the dispersion of the paired Huygens' resonances is greater than either resonance. At vanishing damping, indicated by the dotted line on both (c) and (d), the dispersion of the single resonance and its fluctuation is maximized. The same amount of GD for the paired resonances, on the contrary, can be found at a larger damping, indicated by the solid lines. The corresponding GDD is much smaller compared to the case of single Huygens' resonance, indicating a very small fluctuation of GD in the case of paired resonances. In other words, the paired resonances provide larger and more constant GD modification. Such mechanism is suitable for dispersion-compensated metasurface design where a linear phase delay is needed.

In practical applications, the required dispersion correction is non-uniform in space and one needs a spatially varying dispersion profile on the metasurface. For example, to design a metasurface for grating dispersion correction, an array of Huygens' meta-atoms are arranged in the direction of dispersion, as shown in Fig. S2 in Note D in the SI. As shown by the comparison in Fig. 3 (a) and (b), single Huygens' resonance displays poor phase linearity at large phase delays, indicated by the deviation of edges from the dashed lines. In contrast, the paired resonances can produce quasi-linear phase functions, as shown in (c) and (d), required by the proposed color sorter device.

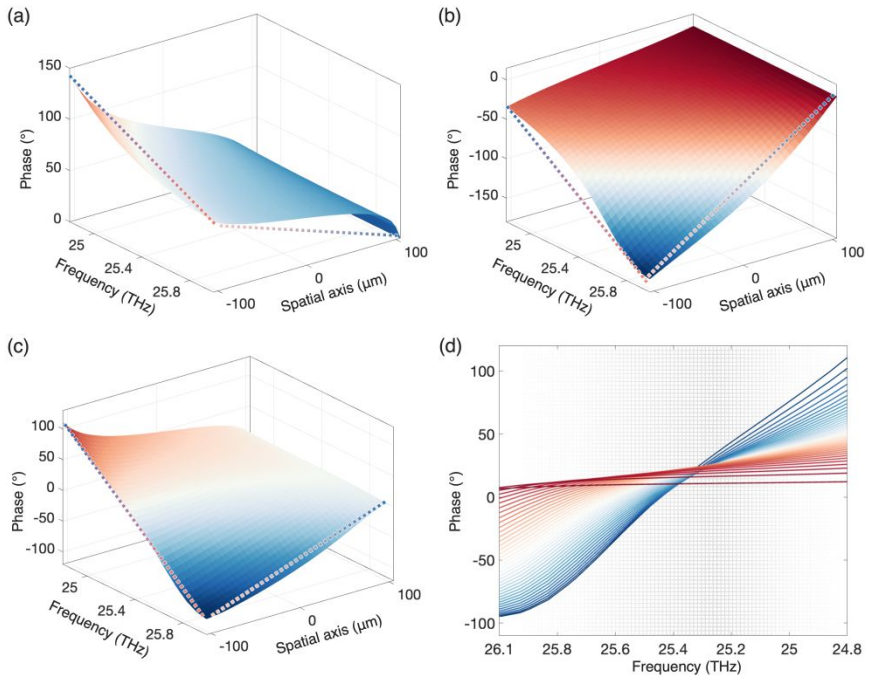

Fig. 3. An example of creating a linear phase function in frequency and space for the proposed dual band color-sorter. (a) Phase function of an array of Huygens' resonances with tuned damping. (b) Phase function of another one-dimensionally aligned Huygens' resonances at adjacent frequency. Neither of the functions in (a) and (b) is linear in frequency and space. (c) The sum of the functions in (a) and (b) displays an improved linearity. (d) The projection of the function in (c) onto the frequency-phase axis.

3. DUAL-BAND COLOR-SORTER DESIGN

A. Design and optimization

To illustrate an example of our approach, a multilayer dielectric metasurface is designed to correct the dispersion and realize achromatic steering of each band. The proposed design of our color-sorter comprises: 1) the use of a transmission grating to roughly redirect the input beam into the designated output angles, and 2) the use of a metasurface to correct the dispersion in each band simultaneously. We employ a transmissive grating to deflect the beams and roughly distribute the waveband close to the designed angles. To begin, the dispersion is calculated via the grating equation, $Gm\lambda = \sin\theta_i + \sin\theta_t$, where $G = |\vec{G}|$ and λ is the incident wavelength. θ_i and θ_t correspond to the incident and diffraction angles, respectively (51). In this design, the energy is diffracted into the 1st diffraction order ($m = 1$). Two infrared sub-bands, 10.5-11.1 μm and 11.6-12.2 μm, in the atmospheric window are chosen. The incident angle θ_i is set to 25°, such that 1) the center wavelengths of the two sub-bands are sufficiently separated and 2) the diffracted beams exit the grating in near normal direction, of which the far-field patterns can be simulated conveniently by invoking the paraxial approximation. In the case of a narrowband input ($\omega \ll \omega_0$), the group delay (GD) ϕ' of the grating is calculated as follows:

$$\phi'(x;\omega) = \frac{\partial\phi(x;\omega)}{\partial\omega}\Big|_{\omega=\omega_0} = -\frac{x}{c_0}\sin\left[\theta_t + \frac{d\theta_t}{d\omega}(\omega-\omega_0)\right] \quad (4)$$

The derivation of Eq. (1) can be found in Note A in the SI. Equation (1) shows that the grating induces a linear change in GD along the direction of the grating vector, $\hat{x} = \vec{G}/|\vec{G}|$, and the wavefront tilts differently with varying wavelength. In our design, the grating constant is G = 41 mm^{-1}. The calculated design specifications are listed in Table 1. The targeting exit angle for each band is determined by the diffraction angle of the central wavelength of the band.

Table 1 Optimized Parameters of the Transmission Grating

Waveband (μm)	10.8 ± 0.3	11.9 ± 0.3
Band center λ_c (μm)	10.8	11.9

Bandwidth $\Delta\lambda$ (μm)	0.6	0.6
Spread angle θ_t at grating output (°)	0.5-1.8	3.0-4.5
ΔGD per length (fs/μm)	0.787	0.818
Target exit angle after correction (°)	1.3	3.5

This metasurface achieves (i) waveband-selective dispersion correction for each band, as indicated by the group dispersion in Table 1, and (ii) high transmission for both bands. The simultaneous control of dispersion is achieved by two pairs of Huygens' resonances in the beam propagation direction. Each pair of resonances is provided by a layer of meta-atoms and for the two sub-bands, four layers of meta-atoms are needed. The schematic of a meta-atom unit cell is shown in Fig. 4 (a). For dielectric Huygens' metasurfaces, the resonance is primarily affected by the diameter (D) and height (H), as well as the unit cell period (P), which arises from the mild inter-particle coupling when high-refractive-index materials are used. To facilitate simpler fabrication processes, H is kept constant for each metasurface layer. Both H and P are jointly optimized in the COMSOL wave optics module to excite Huygens' dipole resonance at the desired wavelength, as indicated by the maximum transmittance at D = 4.3 μm and λ = 12 μm in the example in Fig. 4 (b). Further details of metasurface optimization are included in Note C in the SI. Figure 4 (b) shows the transmittance as a function of wavelength and diameter.

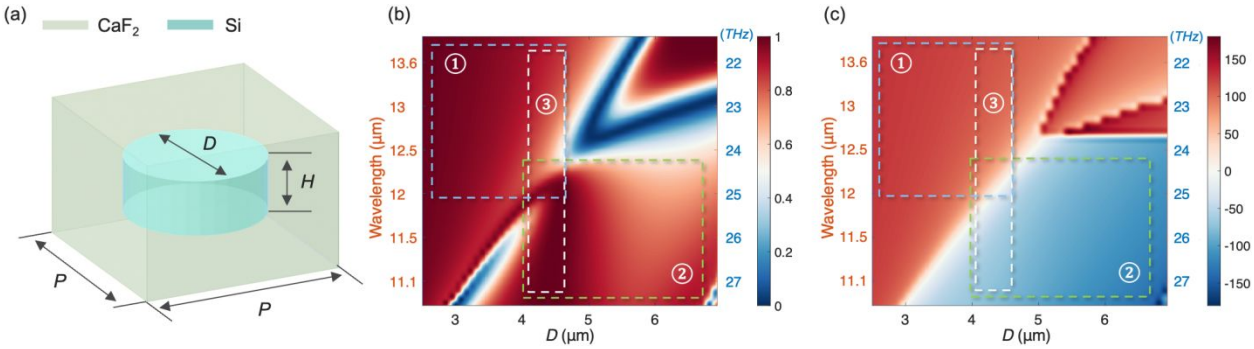

Fig. 4. (a) A schematic of a band sorter metasurface unit cell with a silicon (n=3.41) disk embedded in a CaF_2 (n=1.23) substrate. (b) The transmittance of a unit cell. The high transmittance region where the three dashed boxes overlap indicates the excitation of a Huygens' dipole mode. The dashed boxes 1-3 mark the regions of high transmittance that are used in our design. The boxes of the same index in (c) marks the corresponding phase responses. (b) and (c): axes on the right (blue) show frequencies corresponding to the wavelengths on the left (orange).

The transmittance dips in the lower left corner of Fig. 4 (b) indicates the spectral overlap of the MD and ED modes, giving rise to a typical Fano resonance lineshape. A transmittance peak is observed as the two modes interfere constructively in the forward scattering direction. As D increases from 4.3 μm to 6.2 μm, GD decreases, indicated by box 2 in panel (c). Similarly, GD decreases as D decreases from 4.3 μm, as shown in box 1 in panel (c).

To achieve the desired high transmission, we utilize the three high-transmittance regions in Fig. 4 (b) in a tactical manner. Region 1 refers to the upper left region above the Huygens' resonance in Fig. 4 (b). In this region, longer wavelengths can transmit with high efficiency. Therefore, when the resonance is designed at the lower edge (10.5 μm), both sub-bands can transmit effectively. Conversely, region 2 transmits shorter wavelengths, and its resonance is designed at the upper edge (12.2 μm). Lastly, for the two edges between them, region 3 is used.

The design of the entire metasurface dispersion compensator of our color-sorter is an optimization problem that involves a three-step procedure: 1) determining the resonance wavelengths of the Huygens' meta-atoms, 2) calculating the transmittance with full-wave simulation, and 3) optimizing the layouts of the four metasurface layers. These steps are performed iteratively with empirical guidance during the metasurface design. In step 3, we use a stochastic gradient descent (SGD) optimizer to search for the unit cell parameters that achieve minimal dispersion and better band separation. Further details of our optimization process can be found in Note D in the SI.

B. Results

Following the procedure outlined above, we first identify the geometries of the nanodisks (array periods P, nanodisk heights H, and diameters D) for the four layers of resonators and calculate the corresponding transmittances and phases with full-wave simulations. This library of the nanodisks is then loaded into the optimization program and the far-field radiation patterns are simulated via scalar diffraction with the Fraunhofer approximation. The results of optimization are shown in Fig. 5.

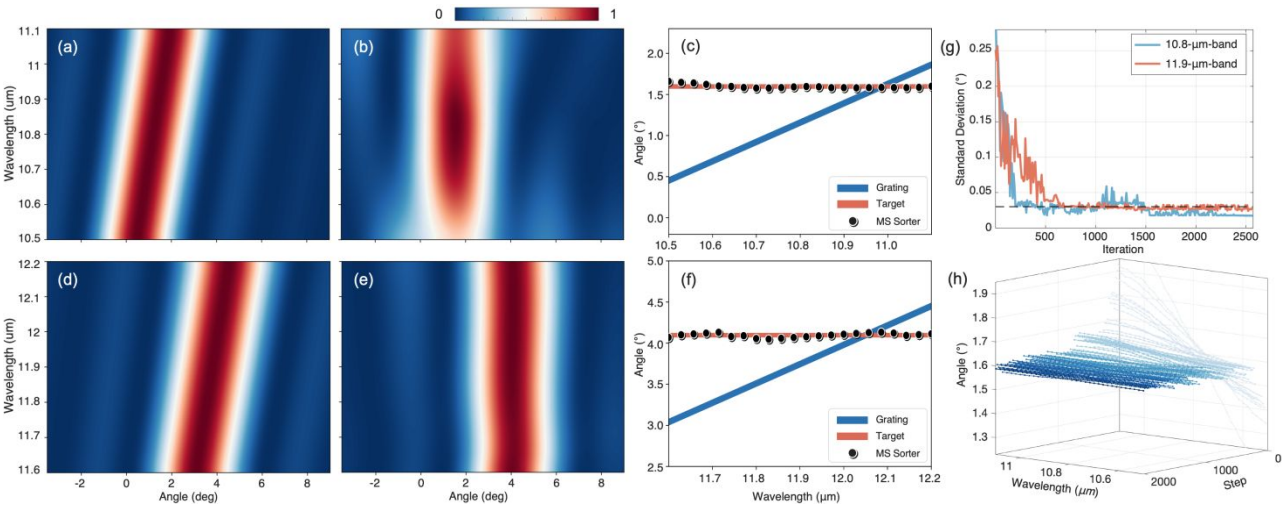

Fig. 5. Sub-band far-field diffraction patterns: (a)-(c) 10.8-μm-band. (d)-(f) 11.9-μm-band. (a) and (d) show the dispersion immediately after the grating. (b) and (e) are the results of dispersion correction. (c) and (f) are the angles of maximum intensity in the corresponding sub-band. (g) Standard deviations of sub-band diffraction angles. (h) Intermediate results of the 10.8-μm-band at the first 2000 steps of (g).

Among them, panel (a) and (d) depict the angular dispersion of a regular diffraction grating, where longer wavelengths are deflected to larger angles. In comparison, the results of dispersion correction with the proposed metasurface device are shown in Fig. 5 (b). The wavelengths in each sub-band exit are bind to a narrow direction, specifically, at an angle of 1.59° for the 10.8-μm-band and 4.11° for the 11.9-μm-band. The location of maximum intensity in both (a) and (b) is displayed in subplot (c), where the blue solid curve represents the dispersion in (a) and the black dotted curve represents that in (b). The angle variation is reduced and each sub-band is deflected to the target angle, indicated by the red solid curve. A similar result is observed in the 11.9-μm-band shown in (f). The root-mean square (RMS) angles of diffraction for the 10.8-μm- and 11.9-μm-band, correspondingly. Information regarding the dispersion angles and transmittances for the working wavebands is tabulated in Table 2.

Table 2 Optimized Waveband Steering Performance

Band (μm)	Centroid (°)		Transmittance (%)	
	Mean	RMS	Mean	Standard deviation
10.8 ± 0.3	1.59	0.023	77	6.3
11.9 ± 0.3	4.11	0.027	58	4.1

Panels (g) and (h) illustrate the intermediate results extracted from one of the many optimizations. In panel (g), the standard deviation values of angle are used to measure the angular uniformity of the broadband diffraction. The two curves are optimized concurrently. The customized merit function punishes imbalance in the two curves. Therefore, despite the separation at the initial iterations, the program eventually reaches an optimal solution. Panel (h) shows the intermediate angular dispersion of the 10.8-μm-band selected per 100 steps. The diffraction angles of the 10.8-μm-band converges to a flat line as the optimization progresses. The computed library of nanodisks is shown in Fig. S1 in Note C and the final optimized design is shown in Fig. S2 in Note D in the SI.

4. DISCUSSION AND CONCLUSION

Using the dipolar modes in the dielectric nanostructures enables precise tuning the dispersion of multiple wavebands without significant interference from nearby resonances. This design strategy can be extended to the dispersion control of more wavebands with even stronger dispersion (52). However, with the increasing total bandwidth of all wavebands, the excitation of higher-order Mie resonances becomes noticeable. These modes, lacking constructive interference in the forward direction, reduce the transmittances of shorter wavelengths. An attempt to create interference among higher-order modes has been made by Kruk et al. (53). However, the design sacrifices the polarization-insensitivity and full phase modulation. We believe that our proposed approach could benefit from investigations into nanoparticle mode engineering, facilitating deliberate enhancement or suppression of specific modes (54, 55). Additionally, near-

field coupling among meta-atoms warrants consideration, particularly when exciting high-order modes with strong radiation sidelobes (50, 56).

In conclusion, we have presented a method for achieving color-sorting using the combination of a grating and a dispersion-correction metasurface. The method leverages a multilayer dielectric Huygens' metasurface to re-combine the diffracted wavelengths from a grating, allowing wavelengths in two wavebands to exit the device at discrete angles. Building upon this approach, we demonstrate a dual-band color-sorting metasurface. The dispersion in each sub-band is reduced by over 90% compared to the grating dispersion. The overall transmittances exceed 57%. Our work provides a new solution for designing multi-band meta-devices with color-sorting capability and facilitating their practical applications.

Author contributions. G. Chen and Dr. J. Zhou contributed equally to the conception and development of the idea; Dr. L. Chen and F. Tian provided theory and numerical simulation support. Dr. Z. Liu supervised this work.

Acknowledgement. The authors thank Leonardo DRS and NASA ESTO for their funding support on Grant #80NSSC20K1671.

Conflicts of interest. The authors declare no conflicts of interest.

Data availability. The data supporting this article have been included as part of the Supplementary Information.

References

1. Papen GC, Blahut RE. Lightwave communications: Cambridge University Press; 2019.
2. James J. Spectrograph design fundamentals: Cambridge University Press; 2007.
3. Brady DJ. Optical imaging and spectroscopy: John Wiley & Sons; 2009.
4. van Ineveld RL, Collot R, Román MB, Pagliaro A, Bessler N, Ariese HCR, et al. Multispectral confocal 3D imaging of intact healthy and tumor tissue using mLSR-3D. Nature Protocols. 2022;17(12):3028-55.
5. Hawkins G, Woods D, Sherwood R, Djotni K. Infrared optical coatings for the EarthCARE Multispectral Imager. Appl Opt. 2014;53(30):6983-92.
6. Liang R. Biomedical optical imaging technologies: design and applications: Springer Science & Business Media; 2012.
7. McClung A, Samudrala S, Torfeh M, Mansouree M, Arbabi A. Snapshot spectral imaging with parallel metasystems. Sci Adv. 2020;6(38):eabc7646.
8. Yu N, Genevet P, Kats MA, Aieta F, Tetienne J-P, Capasso F, et al. Light propagation with phase discontinuities: generalized laws of reflection and refraction. Science. 2011;334(6054):333-7.
9. Yu N, Capasso F. Flat optics with designer metasurfaces. Nature materials. 2014;13(2):139.
10. Cui TJ, Zhang S, Alu A, Wegener M, Pendry J, Luo J, et al. Roadmap on electromagnetic metamaterials and metasurfaces. Journal of Physics: Photonics. 2024.
11. Luo X. Principles of electromagnetic waves in metasurfaces. Science China Physics, Mechanics & Astronomy. 2015;58(9):594201.
12. Zhou J, Qian H, Hu G, Luo H, Wen S, Liu Z. Broadband photonic spin Hall meta-lens. ACS Nano. 2018;12(1):82-8.
13. Tseng ML, Hsiao HH, Chu CH, Chen MK, Sun G, Liu AQ, et al. Metalenses: advances and applications. Adv Opt Mater. 2018;6(18):1800554.
14. Zhou J, Zhang W, Liu Y, Ke Y, Liu Y, Luo H, et al. Spin-dependent manipulating of vector beams by tailoring polarization. Sci Rep. 2016;6(1):34276.
15. Zhou J, Qian H, Luo H, Wen S, Liu Z. A spin controlled wavefront shaping metasurface with low dispersion in visible frequencies. Nanoscale. 2019;11(36):17111-9.
16. Liu Y, Ke Y, Zhou J, Liu Y, Luo H, Wen S, et al. Generation of perfect vortex and vector beams based on Pancharatnam-Berry phase elements. Sci Rep. 2017;7(1):44096.
17. Zhou J, Qian H, Chen C-F, Zhao J, Li G, Wu Q, et al. Optical edge detection based on high-efficiency dielectric metasurface. Proc Natl Acad Sci USA. 2019;116(23):11137-40.
18. Zhou Y, Zheng H, Kravchenko II, Valentine J. Flat optics for image differentiation. Nat Photonics. 2020;14(5):316-23.
19. Chen G, Zhou J, Bopp SE, Zhao J, Liu Z. Visible and near-infrared dual band switchable metasurface edge imaging. Opt Lett. 2022;47(16):4040-3.
20. Xu D, He S, Zhou J, Chen S, Wen S, Luo H. Goos–Hänchen effect enabled optical differential operation and image edge detection. Appl Phys Lett. 2020;116(21):211103.
21. Zhou J, Qian H, Zhao J, Tang M, Wu Q, Lei M, et al. Two-dimensional optical spatial differentiation and high-contrast imaging. Nat Sci Rev. 2021;8(6):nwaa176.
22. Abdollahramezani S, Hemmatyar O, Adibi A. Meta-optics for spatial optical analog computing. Nanophotonics. 2020;9(13):4075-95.
23. Wu Q, Zhou J, Chen X, Zhao J, Lei M, Chen G, et al. Single-shot quantitative amplitude and phase imaging based on a pair of all-dielectric metasurfaces. Optica. 2023;10(5):619-25.
24. Zhou J, Wu Q, Zhao J, Posner C, Lei M, Chen G, et al. Fourier Optical Spin Splitting Microscopy. Phys Rev Lett. 2022;129(2):020801.
25. Kwon H, Arbabi E, Kamali SM, Faraji-Dana M, Faraon A. Single-shot quantitative phase gradient microscopy using a system of multifunctional metasurfaces. Nat Photonics. 2020;14(2):109-14.
26. Pu M, Li X, Ma X, Wang Y, Zhao Z, Wang C, et al. Catenary optics for achromatic generation of perfect optical angular momentum. Sci Adv. 2015;1(9):e1500396.
27. Zheng Z, Xu L, Huang L, Smirnova D, Kamali KZ, Yousefi A, et al. Third-harmonic generation and imaging with resonant Si membrane metasurface. Opto-Electronic Advances. 2023;6(8):220174.
28. Fu R, Chen K, Li Z, Yu S, Zheng G. Metasurface-based nanoprinting: principle, design and advances. Opto-Electronic Science. 2022;1(10):220011.
29. Chen C, Ye X, Sun J, Chen Y, Huang C, Xiao X, et al. Bifacial-metasurface-enabled pancake metalens with polarized space folding. Optica. 2022;9(12):1314-22.

30. Zheng G, Mühlenbernd H, Kenney M, Li G, Zentgraf T, Zhang S. Metasurface holograms reaching 80% efficiency. Nature nanotechnology. 2015;10(4):308-12.
31. Arbabi A, Arbabi E, Horie Y, Kamali SM, Faraon A. Planar metasurface retroreflector. Nat Photonics. 2017;11(7):415-20.
32. Khorasaninejad M, Shi Z, Zhu AY, Chen W-T, Sanjeev V, Zaidi A, et al. Achromatic metalens over 60 nm bandwidth in the visible and metalens with reverse chromatic dispersion. Nano Lett. 2017;17(3):1819-24.
33. Zang W, Yuan Q, Chen R, Li L, Li T, Zou X, et al. Chromatic Dispersion Manipulation Based on Metalenses. Advanced Materials. 2020;32(27):1904935.
34. Wang S, Wu PC, Su V-C, Lai Y-C, Chen M-K, Kuo HY, et al. A broadband achromatic metalens in the visible. Nature nanotechnology. 2018;13(3):227-32.
35. Chen WT, Zhu AY, Sanjeev V, Khorasaninejad M, Shi Z, Lee E, et al. A broadband achromatic metalens for focusing and imaging in the visible. Nature Nanotechnology. 2018;13(3):220-6.
36. Chen WT, Zhu AY, Sisler J, Bharwani Z, Capasso F. A broadband achromatic polarization-insensitive metalens consisting of anisotropic nanostructures. Nat Commun. 2019;10(1):1-7.
37. Li Z, Lin P, Huang Y-W, Park J-S, Chen WT, Shi Z, et al. Meta-optics achieves RGB-achromatic focusing for virtual reality. Sci Adv. 2021;7(5):eabe4458.
38. Xiao X, Zhao Y, Ye X, Chen C, Lu X, Rong Y, et al. Large-scale achromatic flat lens by light frequency-domain coherence optimization. Light: Science&Applications. 2022;11(1):323.
39. Jia R, Gao Y, Xu Q, Feng X, Wang Q, Gu J, et al. Achromatic dielectric metasurface with linear phase gradient in the terahertz domain. Adv Opt Mater. 2021;9(2):2001403.
40. Zhang F, Zhang M, Cai J, Ou Y, Yu H. Metasurfaces for broadband dispersion engineering through custom-tailored multi-resonances. Applied Physics Express. 2018;11(8):082004.
41. Wang S, Wu PC, Su V-C, Lai Y-C, Chu CH, Chen J-W, et al. Broadband achromatic optical metasurface devices. Nat Commun. 2017;8(1):1-9.
42. Chen WT, Zhu AY, Sisler J, Huang Y-W, Yousef KM, Lee E, et al. Broadband achromatic metasurface-refractive optics. Nano Lett. 2018;18(12):7801-8.
43. Sawant R, Bhumkar P, Zhu AY, Ni P, Capasso F, Genevet P. Mitigating Chromatic Dispersion with Hybrid Optical Metasurfaces. Advanced Materials. 2019;31(3):1805555.
44. Arbabi A, Horie Y, Ball AJ, Bagheri M, Faraon A. Subwavelength-thick lenses with high numerical apertures and large efficiency based on high-contrast transmitarrays. Nat Commun. 2015;6(1):1-6.
45. McClung A, Mansouree M, Arbabi A. At-will chromatic dispersion by prescribing light trajectories with cascaded metasurfaces. Light Sci Appl. 2020;9(1):1-9.
46. Li L, Yuan Q, Chen R, Zou X, Zang W, Li T, et al. Chromatic dispersion manipulation based on metasurface devices in the mid-infrared region. Chin Opt Lett. 2020;18(8):082401.
47. Hulst HC, van de Hulst HC. Light scattering by small particles: Courier Corporation; 1981.
48. Evlyukhin AB, Reinhardt C, Seidel A, Luk'yanchuk BS, Chichkov BN. Optical response features of Si-nanoparticle arrays. Physical Review B. 2010;82(4):045404.
49. Decker M, Staude I, Falkner M, Dominguez J, Neshev DN, Brener I, et al. High‐efficiency dielectric Huygens' surfaces. Adv Opt Mater. 2015;3(6):813-20.
50. Liu W, Kivshar YS. Generalized Kerker effects in nanophotonics and meta-optics. Opt Express. 2018;26(10):13085-105.
51. Palmer C, Loewen EG. Diffraction grating handbook. 2005.
52. Raza S. Slow light using magnetic and electric Mie resonances. Opt Lett. 2020;45(5):1260-3.
53. Kruk S, Hopkins B, Kravchenko II, Miroshnichenko A, Neshev DN, Kivshar YS. Invited Article: Broadband highly efficient dielectric metadevices for polarization control. APL Photonics. 2016;1(3):030801.
54. Pedersen JG, Xiao S, Mortensen NA. Limits of slow light in photonic crystals. Physical Review B. 2008;78(15):153101.
55. Baba T, Kawasaki T, Sasaki H, Adachi J, Mori D. Large delay-bandwidth product and tuning of slow light pulse in photonic crystal coupled waveguide. Opt Express. 2008;16(12):9245-53.
56. Gigli C, Li Q, Chavel P, Leo G, Brongersma ML, Lalanne P. Fundamental Limitations of Huygens' Metasurfaces for Optical Beam Shaping. Laser & Photonics Reviews. 2021;15(8):2000448.